

Scanning Lidar Based Atmospheric Monitoring for Fluorescence Detectors of Cosmic Showers

A. Filipčič^{a,b}, M. Horvat^a, D. Veberič^{a,b,*}, D. Zavrtanik^{a,b},
M. Zavrtanik^{a,b}

^a*Nova Gorica Polytechnic, Vipavska 13, POB 301, SI-5001 Nova Gorica, Slovenia*

^b*Jožef Stefan Institute, Jamova 39, POB 3000, SI-1001 Ljubljana, Slovenia*

Abstract

Measurements of the cosmic-ray air-shower fluorescence at extreme energies require precise knowledge of atmospheric conditions. The absolute calibration of the cosmic-ray energy depends on the absorption of fluorescence light between its origin and point of its detection. To reconstruct basic atmospheric parameters we review a novel analysis method based on two- and multi-angle measurements performed by the scanning backscatter lidar system. Applied inversion methods, optical depth, absorption and backscatter coefficient, as well as other parameters that enter the lidar equation are discussed in connection to the attenuation of the light traveling from shower to fluorescence detector.

Key words: backscatter lidar, inversion methods, two- and multi-angle reconstruction, atmospheric optical depth, cosmic showers, fluorescence detectors

PACS: 42.68.Ay, 42.68.Jg, 42.68.Wt, 98.70.Sa

1 Introduction

Contemporary fluorescence experiments (Fly's Eye [1], HiRes [2], P. Auger [3]) studying cosmic rays with energies near 10^{20} eV detect fluorescence light produced along the air-shower volume. As a cosmic-ray induced particle cascade develops in the atmosphere it dissipates much of its energy by exciting and ionizing air molecules. The cascade particles along the shower axis are limited to a narrow lateral distribution where excited nitrogen molecules are fluorescing in the near-UV spectral band. The efficiency of the process is rather small. However, the vast

* Corresponding author.

Email address: darko.veberic@ijs.si (D. Veberič).

number of emitting particles in high energy shower makes this source of radiation highly significant. Ultimately, this electromagnetic (EM) cascade dissipates much of the primary particle's energy. Fluorescence light is emitted isotropically with an intensity proportional to the number of charged particles in the shower. EM component and hence the total number of low energy EM particles is in turn fairly accurately proportional to the energy of the primary particle. Thus, the calorimetric measure of the total EM shower energy [4] is proportional to the integral of EM particle density N_{em} along the shower direction x ,

$$E_{\text{em}} = K \int N_{\text{em}}(x) \, dx \quad (1)$$

with $K \approx 2.2 \text{ MeV cm}^2/\text{g}$, where x is measured in units of longitudinal air density (g/cm^2). E_{em} is a lower bound for the energy of the primary cosmic ray. The lower portion of shower development is usually obscured by the ground so that EM cascade reaching below ground is included by fitting a functional form to the observed longitudinal profile and integrating the function past surface depth. The number of photons N_{ph} reaching fluorescence detector (FD) is proportional to EM particle density $N_{\text{em}}(x)$ at the point of production x , so that in turn

$$N_{\text{em}}(x) \propto \frac{N_{\text{ph}} R^2(x)}{T(x)}, \quad (2)$$

with $R(x)$ being distance between shower point x and FD. Light originating within the shower is certainly affected by the absorption and scattering on molecules and aerosols in the atmosphere. The number of detected photons is thus reduced due to non-ideal atmospheric transmission $T(x) < 1$, where

$$T(x) = \exp \left[- \int_0^x \alpha(r) \, dr \right] = e^{-\tau(x)}, \quad (3)$$

with $\alpha(r)$ volume extinction coefficient along the line-of-sight, and $\tau(x)$ the resulting atmospheric optical depth (OD) to the shower point x .

In this sense, the atmosphere can be treated as an elementary-particle detector. However, weather conditions change the atmospheric transmission properties dramatically resulting in strongly time-dependent detection efficiency. Therefore, an absolute calibration system for fluorescence light absorption is an essential part of FD [5,6].

Eq. (3) is a basis for the fluorescence-detector energy calibration. Apart from the Pierre Auger Observatory, all existing fluorescence-based experiments have suffered from a lack of a sufficient atmosphere monitoring system. Weather conditions in a desert-like atmosphere were expected to be stable enough, so that the standard attenuation-length profile should suffice to reconstruct the total EM shower energy, Eq. (1), with a controllable precision. However, this has turned out not to be the case, especially for rare events with energies above 10^{19} eV . In addition, the

energy reconstruction is obscured by Čerenkov radiation in the lower part of the air-shower which can not be separated from fluorescence. For more than a half of the highest-energy events measured so far the atmosphere properties are not known well enough to accurately reconstruct the primary energy. To be able to provide adequate calibration, one has to measure attenuation at the time of the event in the whole region of the air-shower.

There is also a systematic discrepancy when comparing the cosmic-ray spectra of fluorescence experiments with ground arrays. Their compatibility can be established only with a shift in energy and flux of one or the other. As in the case of fluorescence detectors, ground arrays have their own problems with the energy determination and are much more dependent on air-shower simulations. At present, it is not known whether the discrepancy is due to fluorescence-detector or ground-array method, or both. Therefore, it is of utmost importance to have *in situ* atmosphere monitoring system which is working coherently with a fluorescence detector.

To lower primary cosmic ray energy uncertainties, the volume extinction coefficient $\alpha(r)$ thus has to be well estimated over almost whole detection volume of FD. In the case of the Pierre Auger Observatory, the detection volume corresponds to ground area of 3000 km² and height of ~ 15 km.

The paper is organized as follows. The first two sections are devoted to introductory material on lidar measurement technique and a description of our specific experimental setup. Then the atmospheric model for simulation of lidar signals is presented and the signals are evaluated by two well established inversion methods. Results of the inversions are compared to the input model and conclusions on their applicability are drawn. Next, improved approaches to FD calibration based on scanning lidar system are proposed and evaluated on real data obtained with our experimental setup.

2 Lidar system

One of the most suitable calibration setups for FD is the backscattering lidar system, where a short laser light pulse is transmitted from FD position in the direction of interest. With a mirror and a photomultiplier tube, backscattered light is collected and recorded as a function of time, i.e. as a function of backscatter distance. Note that light from the lidar source traverses both directions, so that in case of matching laser and fluorescence light wavelength, OD for lidar light sums to twice the OD for fluorescence. The lidar equation [11] describes the received laser power $P(r)$ from distance r as a function of volume extinction coefficient $\alpha(r)$ and backscattering

coefficient $\beta(r)$,

$$P(r) = P_0 \frac{ct_0}{2} \beta(r) \frac{A}{r^2} e^{-2\tau(r)}. \quad (4)$$

P_0 is the transmitted laser power and A is an effective receiving area of the detector, proportional to the area of the mirror and proportional to an overlap between its field of view with the laser beam. t_0 is laser pulse duration. As seen from Eq. (2), measurement precision of α and corresponding τ directly influences the precision of primary particle energy estimation.

Simple as it may look, the lidar equation (4) is nevertheless difficult to solve for two unknown variables, $\alpha(r)$ and $\beta(r)$. All existing analysis algorithms (Klett [7], Fernald [8], and their respective variations) reviewed in one of the following sections are based on an experimental setup with static beam direction. This leads to ambiguity in determination of $\alpha(r)$ and $\beta(r)$ which can not be resolved without additional assumptions about atmospheric properties. At the FD experimental sites the atmosphere can be assumed to be almost horizontally invariant. In this case, there is an additional constraint when comparing signals coming from different directions, which solves the lidar equation for $\alpha(r)$ and $\beta(r)$ unambiguously. Even at this point, it can be stated that the need for steerable (scanning) lidar setup is unavoidable for proper solution of lidar equation.

3 Experimental setup

The lidar system used for verification of the analysis method is based on the Continuum MiniLite-1 frequency tripled Nd:YAG laser, which is able to transmit up to 15 shots per second, each with energy of 6 mJ and 4 ns duration (1.2 m). The emitted wavelength of 355 nm is in the 300 – 400 nm range of fluorescence spectrum. The receiver was constructed using 80 cm diameter parabolic mirror with focal length of 41 cm. The mirror is made of aluminum coated pyrex and protected with SiO₂.

The backscattered light is detected by a Hamamatsu R7400 photomultiplier with operating voltage up to 1000 V and gain of 10⁵ to 10⁶. To suppress background, a broadband UG-1 filter with 60% transmittance at 353 nm and FWHM of 50 nm is used. The distance between laser beam and the mirror center is fixed to 1 m, and the system is fully steerable with 0.1° angular resolution.

The signal is digitized using a three-channel LICEL transient recorder TR40-160 with 12 bit resolution at 40 MHz sampling rate with 16k trace length combined with 250 MHz photon counting system. Maximum detection distance of the hardware is thus, with this sampling rate and trace length, set to 60 km. However, in real measurements, atmospheric features up to 30 km only are observed. LICEL is operated

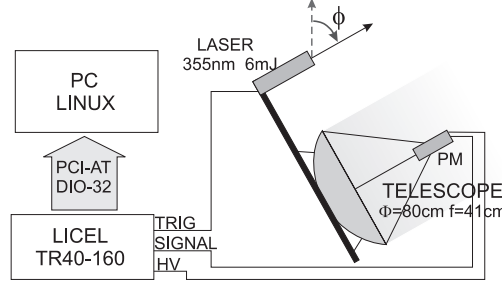


Figure 1. Schematic view of the lidar system. A mirror of 80 cm diameter and a UV-laser head are mounted on the steerable mechanism. The LICEL TR40-160 receives the trigger from the laser and the signal from Hammamatsu R7400 phototube. The Linux-PC controls the LICEL digitizer through PCI-DIO-32HS Digital Input/Output card. The steering motors are controlled through RS-232 port. Zenith angle is denoted by ϕ .

using a PC-Linux system through a National Instruments digital input-output card (PCI-DIO-32HS) with Comedi drivers [9] and a ROOT interface [10].

4 Lidar simulation with specific atmospheric model

In a low opacity atmosphere the attenuation and the backscattering coefficient can be written as a sum of contributions from two independent components,

$$\alpha(h) = \alpha_m(h) + \alpha_a(h), \quad (5a)$$

$$\beta(h) = P_m(180^\circ)\alpha_m(h) + P_a(180^\circ)\alpha_a(h). \quad (5b)$$

where α_m and α_a correspond to molecular and aerosol attenuation, respectively. The aerosol phase function $P_a(180^\circ)$ for backscattering has, apart from the wavelength, also a strong dependence on the optical and geometrical properties of the aerosol particles. Nevertheless, at wavelength of 355 nm, values in the range 0.025 and up to 0.05 sr^{-1} can be assumed [11] for aerosol phase function $P_a(180^\circ)$. The angular dependence of molecular phase function is defined by the Rayleigh scattering theory, where $P_m(180^\circ) = 3/8\pi \text{ sr}^{-1}$.

For simulation purposes, the elevation dependence of the extinction coefficients is modelled as following,

$$\alpha_m(h) = \frac{1}{L_m} e^{-h/h_m^0}, \quad (6a)$$

$$\alpha_a(h) = \frac{1}{L_a} \begin{cases} 1, & h < h_x \\ e^{-(h-h_x)/h_a^0}, & h \geq h_x. \end{cases} \quad (6b)$$

where L_m and L_a are the molecular and aerosol attenuation lengths at ground level, and h_m^0 and h_a^0 are the molecular and aerosol scale height, respectively. An additional mixing height h_x is set up for aerosols, assuming uniform concentration near

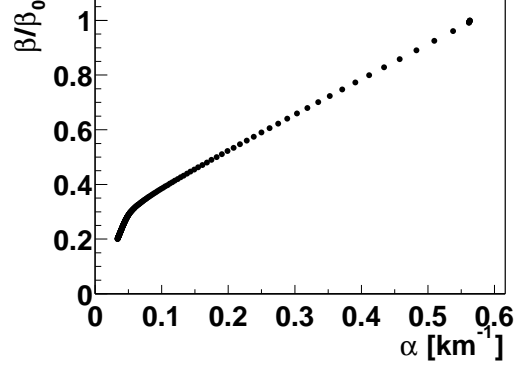


Figure 2. Extinction-backscatter plot ($\alpha\beta$ diagram) for the model atmosphere in Eq. (6).

the ground level and continuous transition into exponential vanishing for $h > h_x$. The following values of the parameters are used: $L_m = 15$ km, $h_m^0 = 17.5$ km, $L_a = 2$ km, $h_x = 0.8$ km, and $h_a^0 = 1.4$ km.

The atmospheric model, Eq. (6), serves as a testing ground for two widely used reconstruction methods presented in the next section. A comparison with reconstruction of the real atmosphere yields insight into the common problems of the lidar field. The Poissonian statistics of photon counting and multiplying, background noise, and effects of digitalization have been taken into account in the generation of the simulated lidar signals and under inspection match those observed in the real lidar power returns.

Model in Eq. (6) is a valid approximation to the atmospheric conditions found in real experiments. Although the vertical variation of aerosol and molecular densities is quite simple, the model still produces a non-trivial relation between total attenuation α and total backscattering coefficient β . Therefore, the dependence of β as a function of α , shown in Fig. 2, cannot be well approximated by some simple functional form.

5 Reconstruction of a 1D atmosphere

Concentrating on a single shot lidar measurement, the optical properties obviously have to be reconstructed in a 1D subspace of the atmosphere. Rewriting the lidar equation (4),

$$P(r) = B \frac{\beta(r)}{r^2} e^{-2\tau(r)} \quad (7)$$

where the effective aperture of the system is gathered in the constant B , an auxiliary S -function can be introduced,

$$S(r) = \ln \frac{P(r)r^2}{P(r_0)r_0^2} = \ln [\beta(r)/\beta_0] - 2\tau(r; r_0). \quad (8)$$

Note that $\tau(r; r_0) = \int_{r_0}^r \alpha(r') dr'$ corresponds to atmospheric OD between r_0 and r .

5.1 Klett inversion

Apart from the experimentally measured lidar power return $P(r)$, in Eq. (7) there are two unknown quantities, β and α (or equivalently τ), preventing the unique solution of the lidar equation. Nevertheless, a simple, and sometimes physically meaningful, assumption of proportionality between backscattering and extinction,

$$\beta(r) \propto \alpha^k(r), \quad (9)$$

allows for the transformation of the integral Eq. (8) to the corresponding Bernoulli's differential equation with an existing analytical solution. Direct application of the solution (forward inversion) is numerically unstable, in some cases singular, and highly sensitive to the signal noise [7,12]. Klett's reformulation [7] of the solution (backward inversion) avoids these problems. The lidar backward inversion algorithm proceeds from the far point of the measured signal r_f to the near end,

$$\alpha(r; \alpha_f) = \frac{e^{S(r)/k}}{e^{S_f/k} / \alpha_f + \frac{2}{k} \int_r^{r_f} e^{S(r')/k} dr'}, \quad (10)$$

where $S_f = S(r_f)$, and $\alpha_f = \alpha(r_f)$ is an estimate for the attenuation at the far end of the data set. The reconstructed attenuation $\alpha(r; \alpha_f)$ is still a one-parameter function of the unknown boundary attenuation value α_f , so that independent measurement, or suitable approximation, is needed at the reference distance r_f . OD can be expressed directly from Eq. (10),

$$\tau(r; r_0, \alpha_f) = \frac{k}{2} \ln \left[\frac{k e^{S_f/k} + 2\alpha_f \int_{r_0}^{r_f} e^{S(r')/k} dr'}{k e^{S_f/k} + 2\alpha_f \int_r^{r_f} e^{S(r')/k} dr'} \right]. \quad (11)$$

Klett's inversion method depends rather strongly on the assumed power law proportionality in Eq. (9). In Fig. 3, a failure of this approximation is demonstrated for the specific atmospheric model used for our simulations. The local value of the exponent,

$$k = \frac{\alpha}{\beta} \frac{d\beta}{dr} \left[\frac{d\alpha}{dr} \right]^{-1}, \quad (12)$$

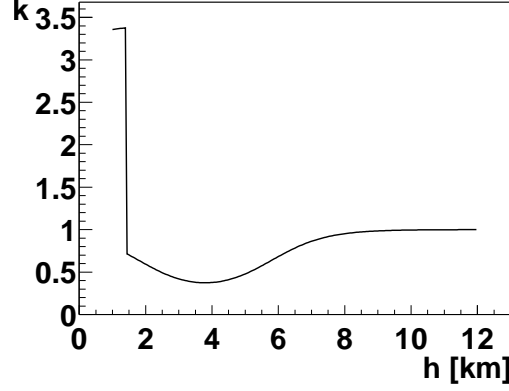


Figure 3. Effective power k in Eq. (9) as obtained from the model atmosphere in Eqs. (5) and (6). Note that the discontinuity at $h_x = 1.4$ km arises due to aerosol part of the model, up to where aerosol concentration is kept constant.

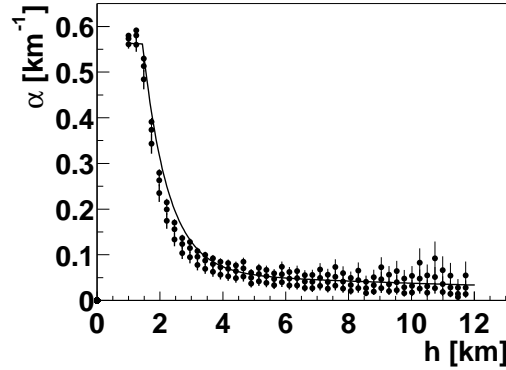


Figure 4. Reconstructed attenuation $\alpha(h)$ from Klett's inversion of the simulated vertical shot data as obtained by different boundary values α_f . Solutions with 0.5, 1, and 2 times the correct α_f are plotted with dots. The actual model α profile is drawn with solid line. Assuming range-independent (constant) Klett's k , the best agreement between the reconstructed and actual profile is achieved for $k \approx 0.5$, therefore this value is used for all tree plots.

is shown to possess substantial range dependence. The main reason for failure of the power law proportionality stems from the inequality of the molecular and aerosol phase functions, $P_m(180^\circ)$ and $P_a(180^\circ)$, rendering the α and β relationship dependent on the particular magnitude of both quantities, and consequently range dependence (see Fig. 2). Therefore, the best value of k must be chosen using some *ad hoc* criterion.

Analyzing results in Fig. 4, presenting Klett inversion of simulated lidar signals, it seems that the closest reconstruction of the model profile is achieved with $k \approx 0.5$. From Fig. 3, showing local exponent k obtained with use of Eq. (12), it can be seen that $k \approx 0.5$ is observed only in small interval around 4 km whereas at other places it is substantially larger. For $r > 8$ km, dominated by molecular scattering it, slowly approaches the value of 1, most commonly adopted in the literature. Nevertheless, as can be seen in Fig. 5, reconstruction of OD with $k = 1$ totally fails to reproduce

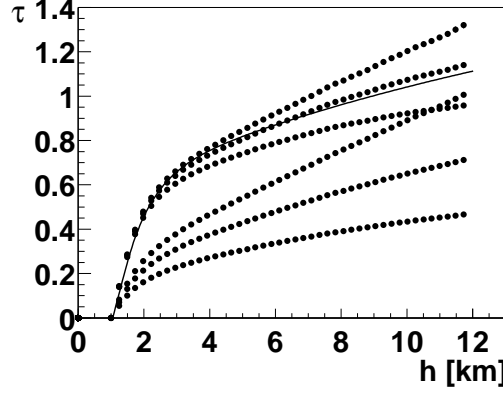


Figure 5. Reconstructed optical depth $\tau(h; h_0)$ as obtained from Klett's inversion in Fig. 4 (with 0.5, 1, 2 times the correct boundary α_f). Upper three curves, with different α_f , are obtained using $k = 0.5$ and lower three with the most frequently used $k = 1$. The actual τ profile from our model is drawn with solid line and is seen to be well approximated by the middle curve with $k = 0.5$.

the correct answer. Surprisingly, in case of this specific atmospheric model the most authentic result is obtained with $k \approx 0.5$.

Another drawback of the Klett's method is estimation of the extinction α_f at the far end of the lidar return. In the case that r_f corresponds to a highly elevated point, approximation $\alpha_f \equiv \alpha_m(r_f)$, i.e. the extinction at that point is dominated by the molecular scattering, yields quite reasonable results [13] with qualitative convergence to the correct α -profile. In general, for optically dense atmosphere (e.g. presence of moderate haze) convergence of the Klett's method is far more rapid as in clear, optically thin case. However, sites for FD are usually chosen at locations with clear and cloudless atmosphere. For horizontal lidar measurements (zenith angle $\phi = 90^\circ$) in a horizontally invariant atmosphere, α_f can be estimated as the one that minimizes extinction deviations from a constant value [13,14], i.e. minimizes the functional $\int_{r_0}^{r_f} [\alpha(r') - \alpha_f]^2 dr'$.

5.2 Fernald inversion

Since the concentration of the molecules depends solely on the thermodynamic parameters of the atmosphere, the Rayleigh scattering on molecules is modeled separately on a basis of the meteorological data. $\alpha_m(r)$ acquired in that way is inserted in Eq. (5). With an estimate for the molecular and aerosol backscattering phase fraction, $F = P_m(180^\circ)/P_a(180^\circ)$, and modified S -function

$$\tilde{S}(r) = S(r) + 2(F - 1) \int_r^{r_f} \alpha_m(r') dr', \quad (13)$$

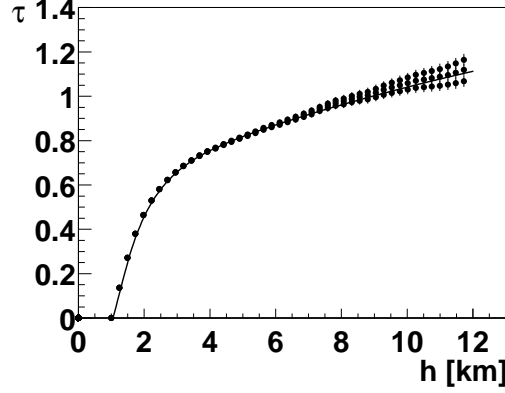


Figure 6. Fernald inversion of simulated lidar signal. The correct result is drawn in solid line. The three data sets are inversions with $\alpha_a(r_f) = 0$ and $\pm\alpha_m(r_f)/2$. The phase fraction F is kept equal to the value used for generation of simulated lidar returns.

the lidar equation can be solved for aerosol part $\alpha_a(r)$ following the same steps as in Klett's version,

$$\alpha_a(r) = -F\alpha_m(r) + \frac{e^{\tilde{S}(r)}}{e^{\tilde{S}_f}/\tilde{\alpha}_f + 2 \int_r^{r_f} e^{\tilde{S}(r')} dr'}, \quad (14)$$

with $\tilde{\alpha}_f = F\alpha_m(r_f) + \alpha_a(r_f)$ and $\tilde{S}_f = \tilde{S}(r_f) = S(r_f)$. In the same way OD is expressed as

$$\begin{aligned} \tau(r; r_0, \tilde{\alpha}_f) = & \frac{1}{2} \ln \left[\frac{e^{\tilde{S}_f} + 2\tilde{\alpha}_f \int_{r_0}^{r_m} e^{\tilde{S}(r')} dr'}{e^{\tilde{S}_f} + 2\tilde{\alpha}_f \int_r^{r_m} e^{\tilde{S}(r')} dr'} \right] + \\ & + (1 - F) \int_{r_0}^r \alpha_m(r') dr'. \end{aligned} \quad (15)$$

Note that the Fernald procedure relies on three independently supplied parameters: (i) an accurate estimate of molecular part of the scattering $\alpha_m(r)$ along the whole range of interest, (ii) total extinction at the far end $\tilde{\alpha}_f$, and (iii) proper approximation for phase fraction F . As predicted by the Mie theory, it is quite difficult to obtain reasonable values for the latter. As for $\tilde{\alpha}_f$, conclusions are similar to those of Klett's α_f .

In Fig. 6 Fernald's inversion of simulated lidar return is shown for different input values of $\alpha_a(r_f)$ that enter total extinction $\tilde{\alpha}_f$. For upward pointing lidar measurements vanishing aerosol concentration can be assumed at the far end of atmosphere, i.e. $\alpha_a(r_f) = 0$. To test the sensitivity of the reconstructed OD on this assumption, data sets with $\alpha_a(r_f) = \pm\alpha_m(r_f)/2$ and therefore $\tilde{\alpha}_f = (F \pm 1/2)\alpha_m(r_f)$, are also plotted. $P_a(180^\circ) = 0.025 \text{ sr}^{-1}$ is used in the expression for phase fraction F . Comparing to the Klett's method, which does not separate aerosol and molecular scattering, it is not surprising that the variation of Fernald's results on boundary parameters is somewhat weaker. Pinning the molecular part of scattering undoubtedly stabilizes OD profiles obtained. Nevertheless, Fernald's inversion still relies heav-

ily on additional external parameters that are usually difficult, if not impossible, to measure.

6 Horizontally invariant atmosphere

Fluorescence detectors for cosmic showers are usually placed at locations with specific atmospheric conditions. In case of the Pierre Auger Observatory, the FD cameras are covering the lower part of the atmosphere over an almost perfect 3000 km² plane 1500 m above the sea level with remarkable fraction of cloudless days. Due to the high elevation and dry inland climate, an optically thin atmosphere is expected. But, as noted before, in this case convergence of Klett's method is slower and can lead to erroneous estimates of OD. Based on that, and other peculiar problems of the well established lidar inversion methods, a new approach with fewer *a priori* or hard-to-estimate input parameters is needed. Since the lidar equation is not uniquely solvable, a minimal set of assumptions needed for inversion has to be reconsidered. For a typical FD site it is quite reasonable to assume weak horizontal variation of the atmospheric optical properties. That is even more true for the huge plane mentioned above, with hardly any changes in elevation and vegetation coverage. Since the FD is exclusively operating at night, only atmospheric conditions at that time have to be considered. The mean night wind speeds do not exceed 12 km/h [15], so that particularly thin layer of aerosols close to the ground is expected. At night, it is also expected that there will be a low probability for formation of convective types of atmospheric instabilities.

6.1 Two-angle reconstruction

Under the moderate assumptions presented above, optical parameters of atmosphere that enter the lidar equation (7) can be assumed to possess only vertical variations, while being uniform and invariant in the horizontal plane.

Thus, it makes sense to rewrite the range dependent S -function in Eq. (8) in terms of height h and geometric factor $\xi = 1/\cos\phi = \sec\phi$, when lidar shots with zenith angle ϕ are considered. The S -function becomes

$$S(h, \xi) = \ln [\beta(h)/\beta_0] - 2\xi \tau(h; h_0) \quad (16)$$

with “vertical” OD $\tau(h; h_0) = \int_{h_0}^h \alpha(h') dh'$ and $\beta_0 = \beta(h_0)$. After measuring two S -functions at different zenith angles $\xi_1 = 1/\cos\phi_1$ and $\xi_2 = 1/\cos\phi_2$ and height h , Eq. (16) can be solved for the vertical OD,

$$\tau(h) = -\frac{1}{2} \frac{S(h, \xi_1) - S(h, \xi_2)}{\xi_1 - \xi_2}, \quad (17)$$

and the backscatter coefficient ratio,

$$\frac{\beta(h)}{\beta_0} = \exp \left[-\frac{\xi_2 S(h, \xi_1) - \xi_1 S(h, \xi_2)}{\xi_1 - \xi_2} \right]. \quad (18)$$

Both quantities are directly proportional to the difference of two S -functions at the same height and different angles. Therefore, choosing a small separation between zenith angles, $\xi_1 = \xi$ and $\xi_2 = \xi + d\xi$, a differential form of Eq. (17) can be written,

$$\tau(h) = -\frac{1}{2} \frac{\partial S}{\partial \xi} \Big|_h. \quad (19)$$

Equivalently, the differential form of Eq. (18) can be obtained,

$$\frac{\beta(h)}{\beta_0} = \exp \left[S(h, \phi) - \xi \frac{\partial S}{\partial \xi} \Big|_h \right]. \quad (20)$$

Note that the OD is in that way determined up to the additive constant, and the backscatter coefficient up to the multiplicative factor. Nevertheless, both values should satisfy $S(h_0) = 0$ and $\tau(h_0) = 0$.

Taking into account the Poissonian statistics of collected photons, and neglecting all other sources of measurement uncertainties, a relative error of the obtained OD at some height depends on the lidar system parameters,

$$\frac{\sigma_\tau}{\tau} = \frac{h/h_0}{2\tau\sqrt{N_0\tilde{\beta}}} \cdot \frac{1}{|\xi_1 - \xi_2|} \sqrt{e^{2\xi_1\tau} + e^{2\xi_2\tau}}, \quad (21)$$

as well as relative error of backscatter coefficient

$$\frac{\sigma_\beta}{\beta} = \frac{h/h_0}{\sqrt{N_0\tilde{\beta}}} \cdot \frac{\sqrt{\xi_2^2 e^{2\xi_1\tau} + \xi_1^2 e^{2\xi_2\tau}}}{|\xi_1 - \xi_2|}, \quad (22)$$

where N_0 is number of detected photons in the time interval corresponding to the power return from height h_0 , and $\tilde{\beta} = \beta/\beta_0$.

In Fig. 7, an example of S -functions and their zenith angle variation is presented. All results are obtained from real lidar measurements performed during few November nights in a typical urban atmosphere (GPS location: 46°04'35" N, 014°29'05" E, 312 m above sea level). For fixed primary azimuth angle $\phi_1 = 0^\circ$ and three selected secondary angles $\phi_2 = 38^\circ$, 42° , and 47° results for OD (Fig. 8), backscatter coefficient (Fig. 9), and $\alpha\beta$ diagram (Fig. 10) are obtained from corresponding S -functions in Fig. 7. Due to presence of a thin layer of optically thick haze at $h \approx 3$ km, a drastic change in both OD and backscattering at that height is observed. Since OD is well determined only up to an additive constant, note that the variation of results for different ϕ_2 is easily produced by the inadequate determination of S_0 , in other terms, by variation of atmospheric optical properties at h_0 .

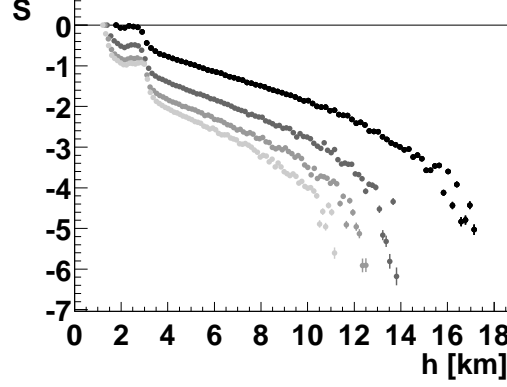


Figure 7. S -function at few angles, $\phi = 0^\circ$, i.e. $\xi = 1$ (upper data set in black), $\phi = 38^\circ$, 42° , and 47° ($\xi = 1.27, 1.35$, and 1.47), in shades of gray (lower three data sets).

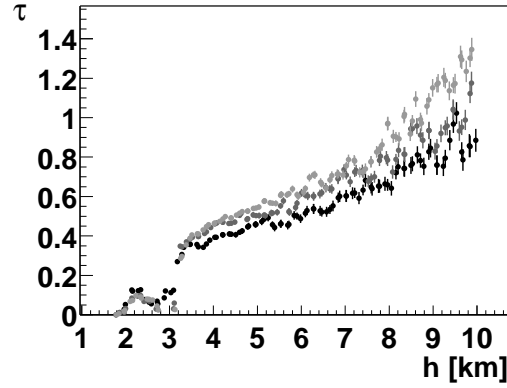


Figure 8. Reconstructed optical depth (OD) τ from three pairs of S -functions. In all pairs, S_1 corresponds to the S -function with $\phi = 0^\circ$ ($\xi = 1$) and S_2 to the S -functions with $\phi = 38^\circ$, 42° , and 47° ($\xi = 1.27, 1.35$, and 1.47), respectively from bottom to top.

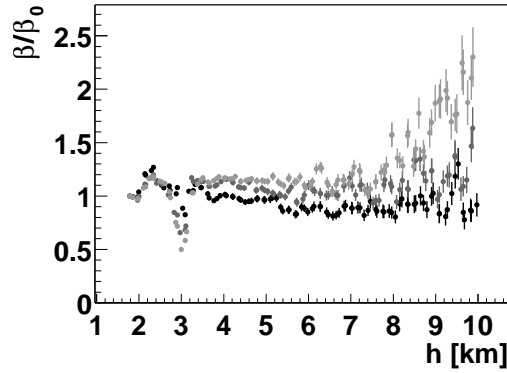


Figure 9. Reconstructed backscatter coefficient $\beta(h)/\beta(h_0)$ from three pairs of S -functions. In all pairs, S_1 corresponds to the S -function with $\phi = 0^\circ$ ($\xi = 1$) and S_2 to the S -functions with $\phi = 38^\circ$, 42° , and 47° ($\xi = 1.27, 1.35$, and 1.47), respectively from bottom to top.

Compatible with a scale height of ~ 18 km, the variation of backscattering in Fig. 9 is slower as found in our model, generating a gradual but still comparable $\alpha\beta$ diagram in Fig. 10.

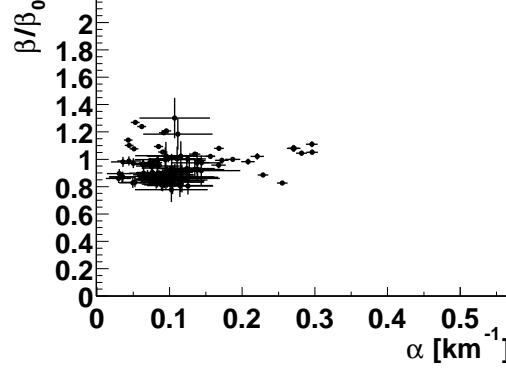


Figure 10. $\alpha\beta$ diagram (extinction-to-backscatter plot) for the pair where S_1 is taken at $\phi = 0^\circ$ and S_2 at $\phi = 38^\circ$. Note that in Fig. 2 the same diagram is plotted also for model atmosphere.

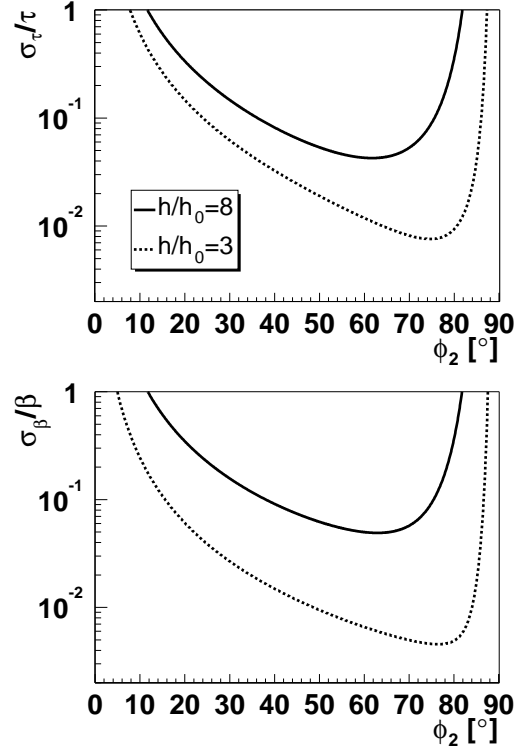


Figure 11. Logarithmic plot of the relative deviation in OD, σ_τ/τ (upper panel), and backscattering coefficient, σ_β/β (lower panel), vs. the second shot angle ϕ_2 , in case that the first shot zenith angle is set to $\phi_1 = 0^\circ$. Values $h/h_0 = 8$, $N_0 = 4 \cdot 10^6$, $\tau = 1$, and $\beta/\beta_0 = 0.6$ corresponding to the far point ($h \approx 8$ km) in Fig. 8 have been assumed for parameters in Eqs. (21) and (22) (solid line). Values $h/h_0 = 3$, $N_0 = 4 \cdot 10^6$, $\tau = 0.4$, and $\beta/\beta_0 = 0.8$ corresponding to the near point ($h \approx 2$ km) are assumed for the dashed curves. Note that $\phi = 60^\circ$ corresponds to $\xi = 2$.

In Fig. 11, a logarithmic plot of the relative error in OD is presented for typical lidar system parameters. First, the angle is fixed to $\phi_1 = 0^\circ$ while the second one, ϕ_2 , is varied from a vertical to an almost horizontal shot. It is hard to avoid the fact that minimum error is produced with evaluation of two quite considerably separated

lidar shots, $\phi_2 \approx 70^\circ$. Even at moderate elevations h this can amount to large spatial separations of the two points of lidar return, and thus the requirement of horizontal invariance easily broken. In the case of an atmosphere, that is slowly horizontally modulated, a more “local” approach to the OD problem is needed.

6.2 Multi-angle reconstruction

For the ideal atmosphere, with true horizontal invariance, the ξ dependence of S -function is particularly simple,

$$S(h, \xi) = \ln[\beta(h)/\beta_0] - 2\xi \tau(h; h_0), \quad (23)$$

with the backscatter coefficient $\ln[\beta/\beta_0]$ as offset, and OD τ as the slope of the resulting linear function in ξ . Therefore, the optical properties of the atmosphere can be alternatively obtained from the analysis of the S -function behavior for scanning lidar measurements. Furthermore, disagreement of the measured $S(\xi)$ profiles from the linear form is a suitable criterion for detection of deviations from the assumed horizontal invariance of the atmosphere.

A generalization of the two-angle equations (19) and (20) to their differential counterparts strongly suggested this way of reconstruction of optical properties, the two-angle method being a mere two-point approximation of the linear function in Eq. (23). Taking into account quite substantial uncertainties in $S(\xi)$ for single angle, the linear fit through many data points seems to yield superior results and the reconstruction is no longer limited to two lidar shots, well-separated in angle. The preferred horizontal invariance is not required to take place across huge atmospheric volumes (as in case of $\phi_1 = 0^\circ$ and $\phi_2 = 60^\circ$ shots), but has to be met only in relatively small arc of interest where the continuous lidar scan is performed.

In the opposite case, when slow variation of atmospheric properties in horizontal plane is allowed, Eq. (19) is similar enough to the renown 1D “slope method”, based on assumption of small variation of $\beta(r)$, or equivalently $d\beta/dr \approx 0$. Bear in mind that in method presented here the variation of β with height can be of any magnitude, as long as there are only modest variations in the horizontal direction.

Opposite to Fig. 7, in Fig. 12 S -function profiles with respect to zenith ξ are drawn for fixed heights, starting with $h = 3.2$ km and up to 7 km with 633 m step. Approximate linear behavior is observed in few arc intervals, with narrow bands of minute atmospheric shifts at $\xi = 1.15$ and 1.38. Since these shifts in profiles disappear when lifting h_0 from 3 km to 3.5 km, they are obviously due to the distortions of atmosphere in the latter interval, feature already observed in Fig. 8.

In Fig. 13 the results of fitting and extraction of OD are similar to the ones in Fig. 8. Note that in both cases OD is obtained relative to the h_0 point, so that the results

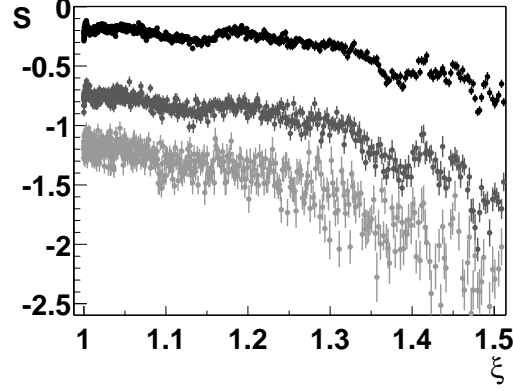


Figure 12. Dependence of S -function on azimuth angle at various heights $h = 3.2$ (black), 5.6 (gray), and 8 km (light gray), while $h_0 = 3$ km. Note that $\xi = 1$ corresponds to $\phi = 0^\circ$, and $\xi = 1.5$ to $\phi = 48^\circ$.

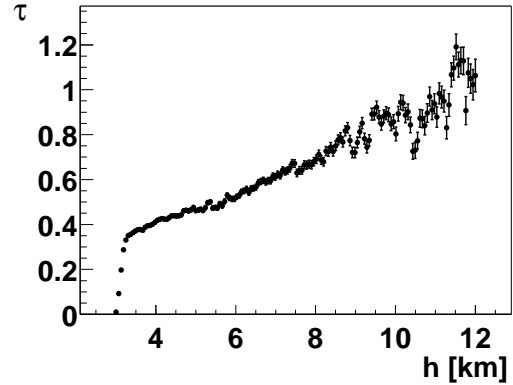


Figure 13. Optical depth τ obtained by linear fits of angle dependence of S -functions in Fig. 12.

may differ up to some additive constant. Therefore, comparing both figures, it is more accurate to concentrate on the same span of OD within the 3.5 km to 9 km interval. Nevertheless, the range of OD results with acceptable error bars is with multi-angle method increased up to 12 km.

The relative error of OD in Fig. 14 is needed for correct estimation of shower energy uncertainty. It is kept below 6% even for the OD from the far points of the range, and below 3% for modest values of OD. Fig. 15, with values for β/β_0 should be compared to Fig. 9.

7 Conclusions

Inversion attempts of simulated lidar returns for atmosphere, modeled by Eqs. (6), show numerous drawbacks of established numerical methods. For instance, Klett's and Fernald's method of section 5.1 and 5.2 do not satisfy the specific requirements of FD calibration. While they may be useful for qualitative reconstruction of atmo-

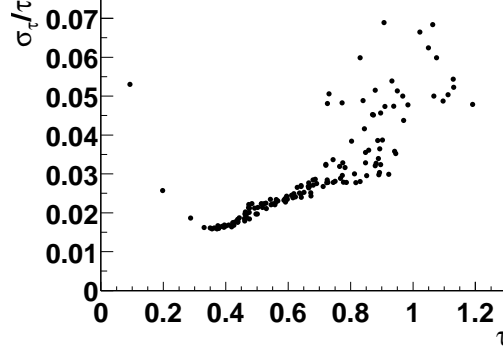


Figure 14. Dependence of relative error in optical depth on depth itself, σ_τ/τ . Data points and uncertainties are from Fig. 13.

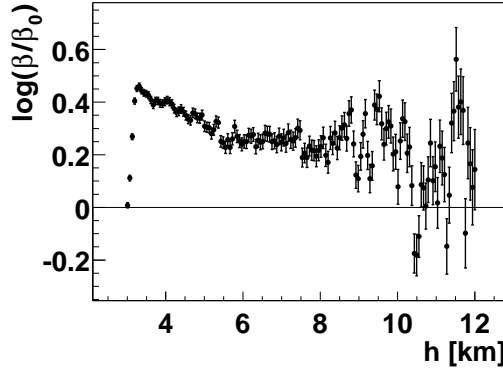


Figure 15. Relative backscattering coefficient $\beta(h)/\beta_0$ from S -functions in Fig. 12.

spheric properties (spatial haze/cloud distribution, cloud base etc.), they are not applicable for absolute assessment of atmospheric transmission properties. There are many reasons for this failure. One of them is certainly strong dependence of obtained inversions on presumed extinction/backscatter functional relation, Eq. (9), in case of Klett's method, and assumed spatial dependence of Rayleigh scattering on molecules in Fernald's case. Another issue is the extraordinarily difficult measurement of far-side extinction rate α_f , needed in Eq. (10), and phase fraction F , Eq. (13). We are therefore forced to find better solutions, even at the expense of adding scanning capabilities to an otherwise rigid lidar setup.

In contrast to that, based on the sole assumption of a horizontally invariant (or at least horizontally slowly varying) atmosphere, the two-, and especially the multi-angle, method presented in section 6, while simple in structure, nevertheless produce reliable quantitative answers with small uncertainties (e.g., see Figs. 8 and 13) to FD calibration questions. As found by our investigation of first-run measurements, the relative error of OD for distances up to 12 km stay well below 6%. This number can be reduced even further by slow angular scanning and fast multiple-shot averaging of lidar returns. Nevertheless, in that case increased interaction between FD and lidar laser source, especially FD blind time, has to be taken into account. Furthermore, concerning the specific form of the atmospheric transmission entering Eq. (2), they offer suitable starting ground for development of methods

that can considerably reduce systematic errors of shower energy E_{em} estimation with fluorescence detectors.

In the case of strict horizontal invariance, both methods deliver exact solutions of the lidar Eq. (4) with accuracy of the results limited only by the quality of the measurement. In that way, they offer reliable framework for study of the notorious *lidar ratio problem* (i.e., extinction to backscatter codependency), widely discussed in the pure lidar community [16]. Since, for example in the case of the Pierre Auger Observatory, where optical properties have to be known over large volumes of atmosphere, and a scanning lidar is therefore a necessity, both mentioned methods represent natural first choice of data analysis.

Acknowledgements

Authors would like to express gratitude to O. Ullaland for the support and encouragement during our work. Authors also wish to thank G. Navarra for assistance with EAS-TOP telescopes. This work has been supported by the Slovenian Ministry of Education, Science, and Sport under program No. P0-0501-1540.

References

- [1] R.M. Baltrusaitis et al., Nucl. Instrum. Methods A **240**, 410 (1985); Phys. Rev. Lett. **54**, 1875 (1985).
- [2] T. Abu-Zayyad et al., Proc. 25th ICRC **5**, 321 (1997); ibid. **5**, 325 (1997); ibid. **5**, 329 (1997).
- [3] D. Zavrtanik, J. Phys. G: Nucl. Phys. **27**, 1597 (2001).
- [4] *Pierre Auger Observatory Design Report*, Second Edition, Auger Collaboration (1997).
- [5] I. Arčon, A. Filipčič, and M. Zavrtanik, Pierre Auger Collaboration note GAP-1999-028, Fermilab (1999).
- [6] D.J. Bird et al., *Atmospheric Monitoring for Fluorescence Detector Experiments* in Proc. 24th ICRC (1995).
- [7] J.D. Klett, Appl. Optics **20**, 211 (1981); ibid. **24**, 1638 (1985).
- [8] F.G. Fernald, Appl. Optics **23**, 652 (1984).
- [9] Comedi, *Linux control and measurement device interface*, <http://stm.lbl.gov/comedi> (2001).

- [10] ROOT, *An Object-Oriented Data Analysis Framework*, <http://root.cern.ch> (2001).
- [11] R.T.H. Collis and P.B. Russell, *Lidar Measurement of Particles and Gases by Elastic Backscattering and Differential Absorption in Laser Monitoring of the Atmosphere*, edited by E.D. Hinkley, p. 88 (Springer, 1976).
- [12] F. Rocadenbosch and A. Comerón, *Appl. Optics* **38**, 4461 (1999).
- [13] M. Horvat, *Measurement of atmospheric optical properties with lidar system*, graduate thesis (Ljubljana, 2001).
- [14] T. Yamamoto et al., *Telescope Array atmospheric monitoring system at Akeno Observatory* in Proc. 27th ICRC (2001).
- [15] P. Bauleo et al., Pierre Auger Collaboration note GAP-1998-041, Fermilab (1998).
- [16] for example see *EARLINET: A European Aerosol Research Lidar Network to Establish an Aerosol Climatology*, Scientific Report for the period Feb. 2000 to Jan. 2001, compiled by J. Bösenberg (2001), <http://lidarb.dkrz.de/earlinet>; F. Rocadenbosch, C. Soriano, A. Comerón, and J.-M. Baldasano, *Appl. Optics* **38**, 3175 (1999) and references therein.
- [17] J.A.J. Matthews, Pierre Auger Collaboration note GAP-2001-046, Fermilab (2001); *ibid.* GAP-2001-051.
- [18] J.A.J. Matthews and R. Clay, *Atmospheric Monitoring for the Auger Fluorescence Detector* in Proc. 27th ICRC (2001).
- [19] B. Dawson, Pierre Auger Collaboration note GAP-2001-016, Fermilab (2001).